Letter

Band gaps and phonons of quasi-bulk rocksalt ScN

Jona Grümbel,* Rüdiger Goldhahn, and Martin Feneberg
Institut für Physik, Otto-von-Guericke-Universität Magdeburg, Universitätsplatz 2, 39106 Magdeburg, Germany

Yuichi Oshima
Research Center for Electronic and Optical Materials, National Institute for Materials Science, 1-1 Namiki, Tsukuba, Ibaraki 305-0044, Japan

Adam Dubroka
Department of Condensed Matter Physics, Masaryk University, Kotlářská 2, 611-37 Brno, Czech Republic

Manfred Ramsteiner
Paul-Drude-Institut für Festkörperelektronik (PDI), Hausvogteiplatz 5-7, 10117 Berlin, Germany

(Received 2 April 2024; accepted 24 June 2024; published 17 July 2024)

ScN is an emerging transition metal nitride with unique physical properties arising from the d electrons of Sc. In this letter, we present the results of optical characterization techniques: spectroscopic ellipsometry, Raman spectroscopy, and photoluminescence measurements of a 40-μm-thick fully relaxed, and only weakly n-type doped ($n = 1.2 \times 10^{18}\,\mathrm{cm}^{-3}$) ScN film deposited by halide vapor phase epitaxy (HVPE) on r-sapphire substrate. Spectroscopic ellipsometry yields an indirect band gap of 1.1 eV, while the lowest direct interband transition is observed at $E_{\mathrm{g,opt}} = 2.16\,\mathrm{eV}$ in the dielectric function. A broad luminescence feature at 2.15 eV is observed, matching this transition. We derive an estimate for the exciton binding energy ($E_{\mathrm{bX}} \approx 14\,\mathrm{meV}$) as well as the Born effective charges $Z^*_{\mathrm{Sc}} = -Z^*_{\mathrm{N}} = 3.81$. In the infrared spectral region, we observe a strong phonon and a weak plasmon absorption. We precisely determine the transverse optical (TO) phonon eigenfrequency ($\omega_{\mathrm{TO}} = 340.7\,\mathrm{cm}^{-1}$), the high frequency dielectric constant ($\varepsilon_\infty = 8.3$), and the static dielectric constant ($\varepsilon_{\mathrm{stat}} = 29.5$). Raman measurements using various excitation energies show resonant multiphonon scattering up to 6LO [sixth-order overtone for longitudinal optical (LO) phonons] for excitation above the optical band gap ($E_{\mathrm{Laser}} > E_{\mathrm{g,opt}}$), where the allowed 2LO scattering is the dominant scattering mechanism for all excitation energies. Their characteristic parameters determined from Lorentzian line shape fitting yield $\omega_{\mathrm{LO}} = 684.5\,\mathrm{cm}^{-1}$ and an increased broadening for higher LO scattering order n.

DOI: 10.1103/PhysRevMaterials.8.L071601

Introduction. ScN is a transition metal nitride with rocksalt (rs) crystal structure ($Fm\bar{3}m$) as the only stable and wurtzite (wz) structure as a metastable phase [1]. It is a promising material for certain applications due to its fundamental characteristics [2]. For example, giant polarization charge densities were predicted for (111)rs-ScN/(0001)wz-GaN interfaces [3], and an improvement of crystalline quality in epitaxial wz-GaN films with rs-ScN interlayers has been achieved [4]. Recently, the ternary alloy system wz-$Sc_xAl_{1-x}N$, which is stable up to 25–35% AlN mole fraction [5,6], attracts high research interest due to piezoelectric [7,8] and ferroelectric properties [9,10] enabling, e.g., wz-$Sc_xAl_{1-x}N$-barrier high-electron-mobility transistor (HEMT) structures via plasma-assisted molecular beam epitaxy (PA-MBE) growth [11]. As a counterpart to wz-AlN, rs-ScN is the binary base material for ternary rs-$Al_xSc_{1-x}N$, which is under current investigation as well [6,8,12] and stable up to ≈55% ScN mole fraction [6].

Early theoretical studies [13,14] concluded that rs-ScN is an indirect semiconductor with its valence band maximum (VBM) located at the Γ point and the conduction band minimum (CBM) located at the X point of the Brillouin zone, which has also been confirmed by more recent studies [15–18]. Experimental attempts including crystal growth and optical characterization were performed by Dismukes *et al.* [19], Travaligni *et al.* [20], and by Gall *et al.* [15,21]. In the past, a very high unintentional free electron concentration usually masked the intrinsic properties of rs-ScN regardless of the growth technique. However, in the last 15 years, there were attempts to grow rs-ScN films with high crystal quality, mainly by halide/hydride vapor phase epitaxy (HVPE) [19,22], sputter epitaxy [23–26] even at room temperature conditions [27], and molecular beam epitaxy (MBE) [28–30], going hand in hand with improved control of the unintentionally introduced free electrons. Sputter grown samples typically exhibit carrier densities $> 1 \times 10^{20}\,\mathrm{cm}^{-3}$ [17,23,24], and MBE grown samples are reported to achieve $5 \times 10^{18}\,\mathrm{cm}^{-3}$ [31]. Oshima *et al.* [22] achieved record $1.2 \times 10^{18}\,\mathrm{cm}^{-3}$ by HVPE. The origin of the unintentional doping is attributed to nitrogen

*Contact author: jona.gruembel@ovgu.de

 ©2024 American Physical Society

vacancies [31–33] and oxygen impurities [34,35]. It was already shown by Dismukes *et al.* [19] and Oshima *et al.* [22] that the thickness of the rs-ScN layer has a massive impact on the structural quality and therefore dominantly determines the carrier concentration. These high unintentional carrier concentrations remain one of the greatest challenges in growth and characterization of rs-ScN.

For application in electrical and optical devices, knowledge of the optical constants of a material is crucial. Also, phonon and luminescence properties may yield relatively quick and nondestructive characterization of semiconductors. In this letter, we provide solid optical parameters, i.e., band gap values, phonon eigenfrequencies and broadenings, optical constants including precisely determined static and high-frequency limits, and Born effective charges of quasi-bulk ScN. Knowledge of these parameter for a bulklike single crystal sets a basis for understanding and design of thin films and heterostructures. Our results reveal several differences to state-of-the-art ScN thin films: most striking, the enhanced above-band-gap absorption, giant amplitude, and narrow linewidth of the infrared (IR) active phonon mode, and strong multiple phonon Raman scattering up to sixth order. Those parameters partially stand in contrast to the properties of traditional III-V semiconductors.

Experimental. For simplification we now use the notation ScN instead of rs-ScN. In this letter, we investigate a (100) oriented, ≈40-μm-thick ScN film deposited by HVPE on r-plane sapphire [22]. X-ray diffraction (XRD) full width at half maximum (FWHM) values are 0.07° and 0.34° for the (200) and (131) reflexes, respectively, indicating relaxation and low dislocation densities. The free carrier concentration of our sample is determined by Hall effect measurements with van der Pauw geometry to be $n = 1.2 \times 10^{18}\,\mathrm{cm}^{-3}$ at room temperature, the corresponding mobility is $264\,\mathrm{cm}^2\,\mathrm{V}^{-1}\,\mathrm{s}^{-1}$. The origin of the free electrons is not clear; however, it is much below the theoretical calculated degeneracy threshold of $\approx 3 \times 10^{19}\,\mathrm{cm}^{-3}$ [18]. Therefore, the sample represents one of the best ScN films currently available. We use optical characterization techniques, namely, spectroscopic ellipsometry (SE) in the IR and near-infrared (NIR)-ultraviolet (UV) spectral range, Raman spectroscopy [including photoluminescence (PL)], and IR reflectivity. Raman spectra were excited by laser wavelengths of 632.8, 532.1, or 472.9 nm. A discussion of spectral resolutions and detailed experimental setups is reported in the Supplemental Material [36].

Theoretical Models. The space group of rs is $Fm\bar{3}m$, the point group $\frac{4}{m}\bar{3}\frac{2}{m}$. Due to the rs structure with two atoms per unit cell, only six phonon branches exist in ScN, where three of them are optical. The eigenfrequencies at the Γ point are predicted to be $632\,\mathrm{cm}^{-1}$ (78.4 meV) for the longitudinal optical (LO) phonon and $365\,\mathrm{cm}^{-1}$ (45.3 meV) for the doubly degenerate transverse optical (TO) phonon modes [37]. Experimental results suggest $2\omega_{\mathrm{TO}} \approx \omega_{\mathrm{LO}}$ [$\omega_{\mathrm{LO}} = 686\,\mathrm{cm}^{-1}$ (85.1 meV), $\omega_{\mathrm{TO}} = 346\,\mathrm{cm}^{-1}$ (42.9 meV)] [38] at the Γ point, which constitutes an even larger LO-TO splitting than theoretically predicted [37]. While first-order Raman scattering in rs-structured crystals is symmetry forbidden, second- and higher-order processes are in general allowed [39] but exhibit a relatively weak scattering efficiency. One way to overcome the small efficiency of *n*th-order phonon scattering is to choose an incident photon energy E_{i}, for which an outgoing resonance condition is fulfilled, i.e., choosing an excitation energy above the optical band gap ($E_{\mathrm{Laser}} > E_{\mathrm{g,opt}}$). The resonance enhancement of multiple phonon scattering in polar materials is expected to be particularly large for LO phonons due to the so-called Fröhlich mechanism [40].

Due to the nonvanishing dipole moment under vibration of Sc^+ and N^- ions, the TO phonon mode is IR active, exhibiting the symmetry T_{1u}. Additionally, in the IR spectral region, one must consider the free carrier absorption for the given carrier concentration ($n > 10^{18}\,\mathrm{cm}^{-3}$). For a single IR-active phonon mode and a Drude contribution, the dielectric function for $\hbar\omega \ll E_{\mathrm{g,opt}}$ is described by

$$\varepsilon(\omega) = \varepsilon_\infty + \frac{S'\omega_{\mathrm{TO}}^2}{\omega_{\mathrm{TO}}^2 - \omega^2 - i\gamma_{\mathrm{TO}}\omega} - \frac{\omega_{\mathrm{P}}^2}{\omega^2 + i\gamma_{\mathrm{P}}\omega}, \quad (1)$$

where $S' = \varepsilon_{\mathrm{stat}} - \varepsilon_\infty$ and $\varepsilon_{\mathrm{stat}}/\varepsilon_\infty$ are the low-/high-frequency limits of $\varepsilon(\omega)$, respectively. Here, with the presence of a plasmon absorption, $\varepsilon_{\mathrm{stat}}$ is the limit $\varepsilon(\omega \to 0)$ without the Drude contribution. The plasma frequency ω_{P} is given by

$$\omega_{\mathrm{P}}^2 = \frac{ne^2}{\varepsilon_0 m_{\mathrm{e,opt}}^*}, \quad (2)$$

where $m_{\mathrm{e,opt}}^*$ is the optical effective mass [41] and n the concentration of free electrons in the conduction band. For ScN, the approximation of a constant ε_∞ does not hold satisfactorily; therefore, we use the model by Shokhovets *et al*. [42]:

$$\varepsilon_{\mathrm{vis}}(\omega) = 1 + \frac{2}{\pi}\left\{\frac{A_{\mathrm{g}}}{2}\ln\left[\frac{E_{\mathrm{h}}^2 - (\hbar\omega)^2}{E_{\mathrm{g}}^2 - (\hbar\omega)^2}\right] + \frac{A_{\mathrm{h}}E_{\mathrm{h}}}{E_{\mathrm{h}}^2 - (\hbar\omega)^2}\right\}. \quad (3)$$

We follow the notation of Ref. [43]. Within this model, ε_∞ is given by $\varepsilon_\infty = \varepsilon_{\mathrm{vis}}(\omega \to 0)$, and ε_∞ in Eq. (1) is replaced by $\varepsilon_{\mathrm{vis}}$ from Eq. (3). Additionally, the LO-TO splitting and ε_∞ yield the Born effective charges Z^*, given by [44,45]

$$\omega_{\mathrm{LO}}^2 - \omega_{\mathrm{TO}}^2 = \frac{(Z^*e)^2}{\varepsilon_0\varepsilon_\infty V_0\mu}, \quad (4)$$

where $Z^* = Z_{\mathrm{Sc}}^* = -Z_{\mathrm{N}}^*$ fulfills the required sum rule, V_0 is the primitive unit cell volume, and $\mu = M_{\mathrm{Sc}}M_{\mathrm{N}}/(M_{\mathrm{Sc}} + M_{\mathrm{N}})$ the reduced mass. The lattice constant of strain-free ScN is well known to be $a = 4.505$ Å [29].

To describe the imaginary part of the dielectric function around the fundamental absorption edge, we use the model by Elliott *et al.* [46]. For the exciton continuum, we have

$$\varepsilon_2^{(\mathrm{con})}(\omega) = \frac{C}{\hbar\omega}\frac{1 + \mathrm{erf}\left[\frac{\hbar\omega - E_{\mathrm{g}}}{\gamma_{\mathrm{g}}}\right]}{1 - \exp\left[-2\pi\sqrt{\left|\frac{E_{\mathrm{bX}}}{\hbar\omega - E_{\mathrm{g}}}\right|}\right]} + \varepsilon_{\mathrm{off}}, \quad (5)$$

where E_{bX} denotes the exciton binding energy, γ_{g} is the empirical width of the exciton continuum absorption, C a constant considering the transition matrix element, and E_{g} the band gap energy [43]. The constant offset $\varepsilon_{\mathrm{off}}$ is added to improve the fit results, as discussed later. In addition, different electronic transitions are assigned to van Hove singularities in the joint density of states (JDOS). From the electronic band structure shown in Fig. 1, we can assume a M_0 critical point (CP) for the direct X transition (at ≈2 eV), a M_1 CP for the direct Γ

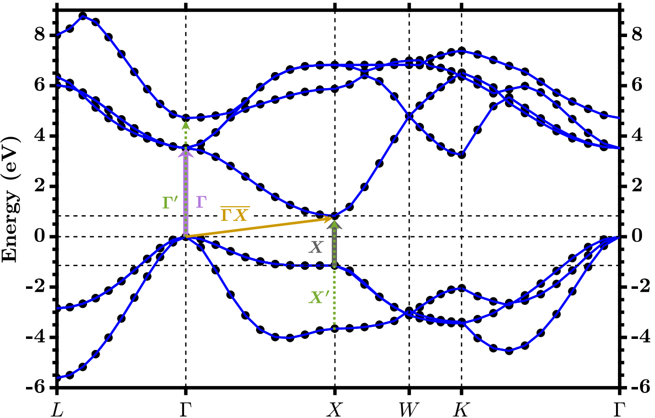

FIG. 1. Numerically determined, exact-exchange-based quasiparticle bandstructure of rs-ScN from Ref. [16] and main critical point transitions.

transition (at ≈4 eV) and a M_0 CP for the direct Γ′ or X' transition (at ≈5.5 eV) to the second conduction or valence band, respectively. For different types of CPs, different line shapes of $\varepsilon(\omega)$ are expected.

Results. Ellipsometric angles and pseudodielectric function. The ellipsometric angles Ψ and Δ shown in Figs. 2(a) and 2(b) are converted to the so-called pseudodielectric function $\langle\varepsilon\rangle$, partially shown in Fig. 2(d). Here, Ψ and Δ are the polarization angle and phase shifts that emerge from the reflection of light with a distinct polarization at an interface. For a cubic crystal, they are linked to the diagonal Fresnel coefficients r_{jj} by

$$\rho = \frac{r_{\mathrm{pp}}}{r_{\mathrm{ss}}} = \tan(\Psi)e^{i\Delta}, \tag{6}$$

and to the pseudodielectric function by

$$\langle\varepsilon\rangle = \sin^2\Phi\left[1 + \tan^2\Phi\left(\frac{1-\rho}{1+\rho}\right)^2\right], \tag{7}$$

where Φ is the incident angle. Here, $\langle\varepsilon\rangle$ would be identical to ε in case of an isotropic, semi-infinite, and perfectly smooth sample.

For photon energies $<(1.1 \pm 0.1)$ eV, the datasets obtained with different angles of incidence do not merge to a single $\langle\varepsilon\rangle$. This threshold can be interpreted as the energy position where incoherent interface reflections become relevant, i.e., the energy of the indirect band gap which is found between Γ and X

FIG. 2. Measured ellipsometric parameters (a) Ψ and (b) Δ for three different incident angles (gray solid) and corresponding point-by-point dielectric function model fit results (red solid) for infrared spectroscopic ellipsometry and ultraviolet spectroscopic ellipsometry. (c) Measured IR reflectivity (red solid), model fit (black solid), and calculated reflectivity from point-by-point fitted ε_1 and ε_2 (red dashed) and (d) pseudodielectric functions $\langle\varepsilon_1\rangle$ (blue) and $\langle\varepsilon_2\rangle$ (orange) from UV-SE.

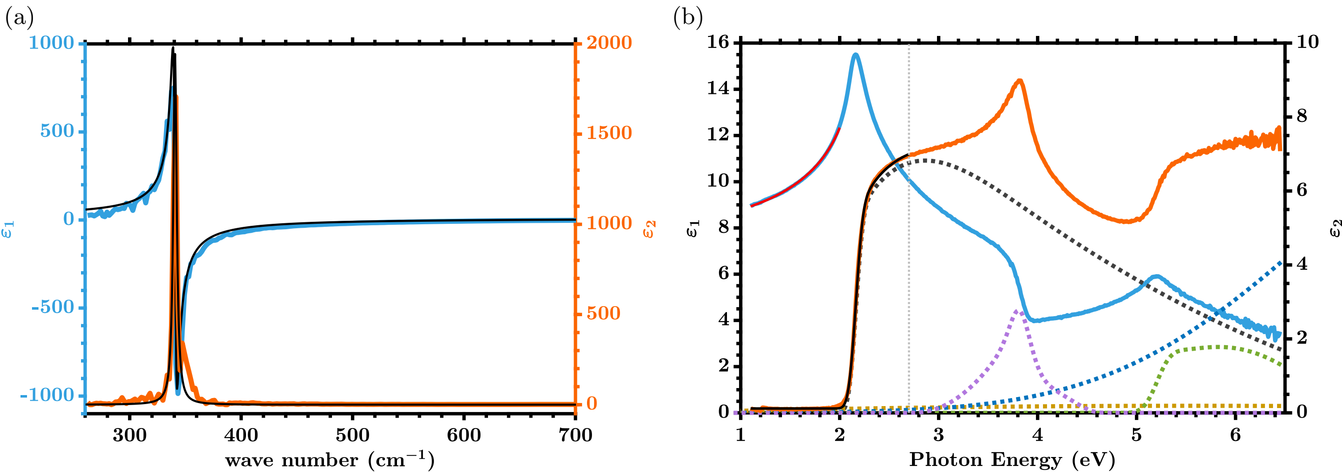

FIG. 3. (a) Real (blue) and imaginary (orange) part of the point-by-point fitted dielectric function derived from infrared spectroscopic ellipsometry and Lorentz-model fit (black lines). (b) Real (blue) and imaginary (orange) parts of the point-by-point fitted dielectric function derived from ultraviolet spectroscopic ellipsometry, Elliott model fit to ε_2 (black line), Shokovets model fit to ε_1 (red line), and different model oscillators (color dotted). The reference line indicates the upper bound (2.7 eV) of the area, where only the direct X transition exhibits $\varepsilon_2 \gg 0$.

points of the Brillouin zone. This indirect band gap energy of (1.1 ± 0.1) eV is in good agreement with earlier results [15,16,18,47]. Due to incoherent backside reflections in the transparent region [0.089 eV(720 cm^{-1})–1.1 eV] the point-by-point fit does not yield reliable results, which is obvious from Figs. 2(a) and 2(b). Therefore, we exclude this spectral range from the analysis of point-by-point fitted dielectric functions. The offset in Ψ and Δ between infrared spectroscopic ellipsometry (IR-SE) and ultraviolet spectroscopic ellipsometry (UV-SE) data is caused by different spot sizes.

NIR-UV dielectric function. To obtain the dielectric function of ScN, we apply a simple bulk model without considering the substrate including the ScN layer and an obligatory roughness effective medium layer for the NIR-UV spectral range (UV-SE), which is 8 nm thick and has a layer/void ratio of 50%. Point-by-point-fitting of the complex refractive index of the ScN layer yields the real and imaginary parts of the dielectric function, which are shown in Fig. 3(b) for the NIR-UV spectral range [point-by-point fit results are shown in Figs. 2(a) and 2(b)]. This dielectric function is decomposed into different empirical functions (generalized parametric semiconductor oscillators provided by the analysis software WVASE32) exhibiting the typical characteristics of different critical point transitions. In Fig. 3(b), these contributions are shown as well.

The characteristic energies of these oscillators are compared with the band structure calculated by Qteish *et al.* [16] (Fig. 1), and very good qualitative agreement is found. The fundamental absorption edge of ScN is located at the X point of the Brillouin zone, in agreement with Gall *et al.* [15] and Haseman *et al.* [48], but in contrast with Saha *et al.* [24]. The energetic ordering of the main transition features in the dielectric function [Fig. 3(b)] corroborates this fact: At ≈2 eV, we find a M_0-like transition, at ≈4 eV, a M_1-type transition, and again, a M_0-type transition at ≈5 eV. The band structure (Fig. 1) reveals the same ordering: The lowest direct CP transition occurs at the X point ($dE_{\text{joint}}/dk > 0$ for all directions, hence M_0 CP) and a second direct CP transition at the Γ point ($dE_{\text{joint}}/dk < 0$ only for the $\overline{\Gamma X}$ direction, hence M_1 CP). The third CP transition could be assigned to two different points: (i) VB(Γ) to second CB(Γ) or (i) second VB(X) to CB(X). Possibly they both appear at around the same energy. The remaining contributions to our model are a general higher-energy contribution [Fig. 3(b), blue dotted] and a small background-like contribution describing the indirect $\overline{\Gamma X}$ transition [Fig. 3(b), yellow dotted].

A quantitative analysis of the dielectric function for $E >$ 1.1 eV reveals the fundamental absorption edge at $E_g =$ 2.16 eV with a width of $\gamma_g = 76$ meV from Elliott's model [Eq. (5)]. Applying Shokhovets' model [Eq. (3)], we obtain $A_g = 7.1$ and $A_h = 27.4$ eV, which precisely yields $\varepsilon_\infty =$ 8.3 ($E_g = 2.16$ eV and $E_h = 5.20$ eV were fixed). The fitted curves and the real and imaginary parts of the dielectric function are displayed in Fig. 3(b). Shokhovets' model was applied only to ε_1 for $E < 2$ eV. Elliott's model is valid only for a single M_0-type VB-to-CB transition. Therefore, the fit was applied to the spectral region of $\varepsilon_2(\omega)$, where all other transitions have $\varepsilon_2 \approx 0$, which is the case for $E < 2.7$ eV [see Fig. 3(b)]. What remains is the indirect absorption edge contribution, which we approximate by a constant offset ε_{off} in Eq. (5). Although we do not observe any discrete exciton state, we obtain the exciton binding energy $E_{bX} = 14$ meV as an estimate. For the transition energies E_Γ and $E_{\Gamma'}$, we determine the inflection points of ε_2 to be $E_\Gamma = 3.75$ eV and $E_{\Gamma'} = 5.20$ eV, in good agreement with the electronic band structure shown in Fig. 1.

Further, we observe a relatively high absolute ε_2 above the fundamental band gap ($\varepsilon_2 \approx 7$ at 3 eV) which yields an absorption coefficient $\alpha = 3.4 \times 10^5$ cm^{-1} at 3 eV, which is significantly larger than that of, e.g., GaN [49] or other common III-V nitrides at ≈1 eV above the absorption onset. Overall, our observations are like those of Dinh *et al.* [50] qualitatively, but our absolute amplitudes of ε_1 and ε_2 are larger by a factor of ≈1.3–1.5. Additionally, we can derive the Born effective charges from our ε_∞ and later determined $\omega_{\text{LO,TO}}$. We have $Z^*_{\text{Sc}} = -Z^*_{\text{N}} = 3.81$ [Eq. (4)], which is well above the expected ionization levels of 3/−3 for Sc/N, respectively, but significantly lower than it was

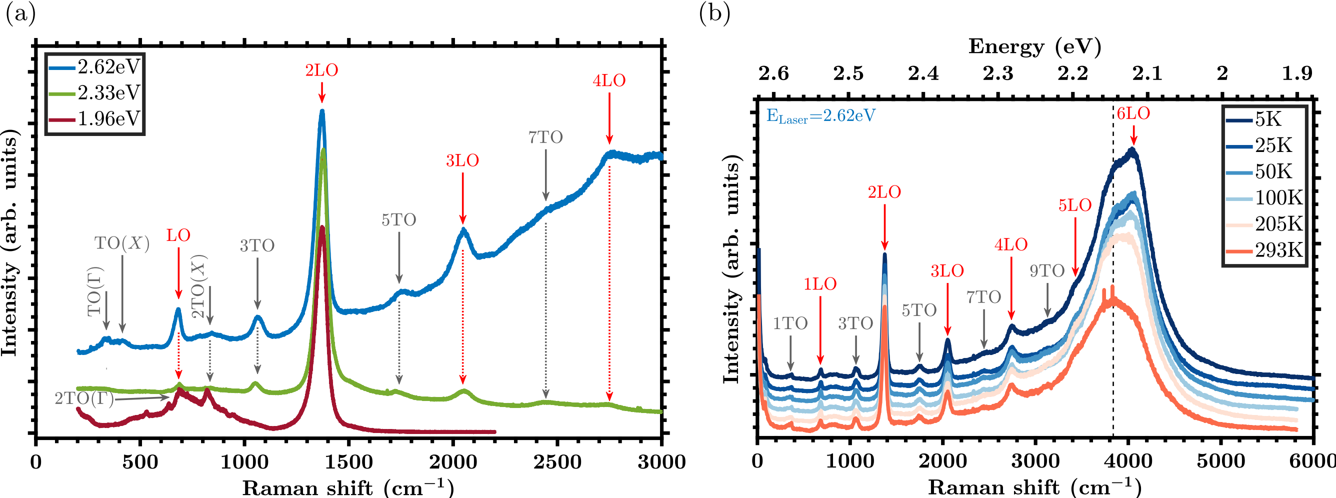

FIG. 4. (a) Room-temperature Raman spectra at three different excitation wavelengths and (b) Raman and photoluminescence (PL) spectra from 5 to 293 K at an incident laser energy of 2.62 eV.

theoretically predicted [51]. This hints toward a strong bonding hybridization, leading to an admixture of N $2p$ and Sc $3d$ states in the highest occupied valence band, which was already shown by theoretical calculations [16]. The same behavior was observed for the related rs-CrN by both theory [52] and experiment ($Z^* = 4.4$) [44].

IR dielectric function. In the IR spectral range, a broad reststrahlenband arising from the phonon absorption and a free carrier absorption for $\omega < 200\,\mathrm{cm}^{-1}$ is observed from IR reflectivity measurements [Fig. 2(c)]. From the model fit [Eqs. (1) and (3)], we determine Drude parameters of $\omega_\mathrm{P} = 1200\,\mathrm{cm}^{-1}$ and $\gamma_\mathrm{P} = 250\,\mathrm{cm}^{-1}$, yielding an effective electron mass of $m_\mathrm{e}^* = 0.07 m_\mathrm{e}$ [Eq. (2)]. This effective electron mass is well below various theoretically calculated [16,18,51] and experimentally determined [17,47] values [$m_\mathrm{DOS} \approx (0.35 \pm 0.05) m_\mathrm{e}$]. In Fig. 2(c), it is obvious that the applied model does not match the data well, especially for wave numbers $<250\,\mathrm{cm}^{-1}$. Therefore, we conclude that the Drude formalism currently does not hold satisfactorily for free electrons in ScN, and the determined plasmon parameters are not trustworthy. Evaluation of the IR-SE data [see Figs. 2(a) and 2(b)] yields more accurate results, but due to the limited spectral range, the plasmon absorption is not detectable.

The point-by-point fitted dielectric function shown in Fig. 3(a) shows a strong phonon absorption with a maximum of $\varepsilon_2 \approx 1700$, and the reflectivity calculated from this dielectric function matches the measured reflectivity well [Fig. 2(c)]. A similar value of ε_2 was reported before [53] and hints toward a partially ionic bond in ScN, which was theoretically predicted by Weinberger *et al.* [13]. A Lorentz fit [Eq. (1) without the Drude contribution] including our fixed $\varepsilon_\mathrm{vis}(\omega)$ [Eq. (3)] from the UV-SE yields a TO frequency of $\omega_\mathrm{TO} = 340.7\,\mathrm{cm}^{-1}$, broadening $\gamma_\mathrm{TO} = 3.7\,\mathrm{cm}^{-1}$, an amplitude $S = 21.2$, and hence, $\varepsilon_\mathrm{stat} = 29.5$. This broadening γ_TO is about twice the selected spectral resolution (see the Supplemental Material [36]). In comparison with common III-V nitride semiconductors such as GaN, the oscillator strength of the TO phonon, and hence $\varepsilon_\mathrm{stat}$, is very high, and thus, semiconducting ScN is a so-called high-k dielectric. The determined TO frequency ($\omega_\mathrm{TO} = 42.24\,\mathrm{meV}$) matches well with the experimentally determined phonon dispersion of Uchiyama *et al.* [$\omega_\mathrm{TO}(\Gamma + \delta k) = 42.9\,\mathrm{meV}$] [38] but is in contrast with several theoretical calculations [37,51] and other experiments [53].

Raman and PL spectra. For Raman and PL measurements, we employed three different incident laser wavelengths: 472.9 nm (2.62 eV), 532.1 nm (2.33 eV), and 632.8 nm (1.96 eV). In Fig. 4(a), the Raman spectra obtained with different excitation wavelengths are shown. These spectra are measured with a better resolution than PL (see the Supplemental Material [36]). For all three incident laser energies, the allowed [39] second-order scattering by two LO phonons (2LO peak) is the dominant scattering process with $\omega_\mathrm{2LO} \approx 1370\,\mathrm{cm}^{-1}$. Although first-order scattering is Raman forbidden, we observe weak first-order Raman scattering for excitation energies of 2.33 and 2.62 eV. Assigning the multiple (nth-order) phonon scattering peaks must be done carefully for $\omega_\mathrm{LO} \approx 2\omega_\mathrm{TO}$, and hence, signals can be undistinguishable. The Raman spectrum at an incident laser energy of 2.62 eV shows nLO scattering up to 4LO [see Fig. 4(a), blue line]. In the same figure, nTO signals are labeled for odd n. Due to $\omega_\mathrm{LO} \approx 2\omega_\mathrm{TO}$, these Raman signals could either be $(2n-1)$TO or nLO + TO peaks. We observe two different first-order TO-related peaks at ≈336 and ≈415 cm^{-1}, with 2.62 eV excitation. They can be assigned to TO(Γ) and TO(X), in good agreement with previous experimentally determined values at Γ ($\omega_\mathrm{TO} = 346\,\mathrm{cm}^{-1}$) and at X ($\omega_\mathrm{TO} = 408\,\mathrm{cm}^{-1}$) points of the Brillouin zone [38].

Changing the laser energy to 2.33 eV yields $E_\mathrm{Laser} \approx E_\mathrm{g,opt} + 2E_\mathrm{LO}$ and hence nearly perfect critical point resonance for the 2LO (and 4TO) scattering. Therefore, all other signals exhibit relatively small intensities. For excitation in the transparent region at 1.96 eV, the condition for the enhancement of multiple-order phonon scattering by outgoing resonances is no longer fulfilled. Indeed, while we still observe a dominant 2LO peak, no higher-order scattering is found [see Fig. 4(a), red line]. Additionally,

TABLE I. Characterization of single and multiple phonon resonant Raman scattering for an incident laser energy of 2.62 eV. Eigenfrequencies ω_0/n, broadening parameters γ, and signal-to-noise ratios (snr) were determined by Lorentzian line shape fitting.

	TO(Γ)	TO(X)	2TO	LO	3TO	4TO	2LO	5TO	6TO	3LO	7TO	8TO	4LO
$\frac{\omega_0}{n}$ (cm^{-1})	336 ± 2	415 ± 2	334.5 ± 2	684.5 ± 2	355.0 ± 0.2	338.8 ± 0.8	689.0 ± 0.5	350.0 ± 0.4	337.5 ± 0.8	686 ± 1	349.4 ± 0.7	342.0 ± 0.6	689 ± 0.8
γ (cm^{-1})	76 ± 6	64 ± 8	40 ± 7	27 ± 4	60 ± 3	59 ± 4	36 ± 4	94 ± 8	75 ± 8	65 ± 6	100 ± 30	30 ± 20	210 ± 20
snr	6.3 ± 0.3	4.0 ± 0.3	9 ± 3	14 ± 4	12.8 ± 0.3	66 ± 8	63 ± 9	6.5 ± 0.3	8 ± 2	10 ± 2	1.3 ± 0.2	0.6 ± 0.3	5.3 ± 0.4

we observe a broad contribution covering various narrower signals ~700 cm^{-1}. The origin of this broad contribution is not known yet. Because we do not expect first-order scattering for the nonresonant excitation at 1.96 eV, we tentatively assign the two features at ≈690 and ≈830 cm^{-1} as 2TO(Γ) and 2TO(X) rather than first-order LO scattering. The 2TO(X) is also weakly visible at other incident laser energies.

For a quantitative analysis, line shape fits are performed using standard Lorentzian-type functions. Due to the luminescence signal, which is located directly at the position of the 2LO line, the spectrum for $E_{\text{Laser}} = 2.33$ eV is impossible to fit unambiguously, and with 1.96 eV excitation, we observe only second-order scattering. Therefore, we choose to model only data recorded with $E_{\text{Laser}} = 2.62$ eV. Results are summarized in Table I, and fit details are reported in the Supplemental Material [36]. From Table I, the dependence of the n-LO broadening γ on the LO-order n is obvious. We observe increasing broadening with higher scattering order n, while the broadening values for the nTO lines scatter ≈40–100 cm^{-1}. An important result is the LO eigenfrequency obtained from fitting the first-order LO signal. We have $\omega_{\text{LO}} = 684.5$ cm^{-1}, in good agreement with earlier experiments ($\omega_{\text{LO}} = 686$ cm^{-1}) [38,53], but in contrast with theoretical calculations ($\omega_{\text{LO}} \approx 630$ cm^{-1}) [37,51] at the Γ point. The phonon lifetime can easily be derived as the inverse phonon broadening as $\tau_{\text{LO}} = (2\pi\gamma_{\text{LO}})^{-1}$. We have $\tau_{\text{LO}} = 0.2$ ps, which is again in perfect agreement with previous experimental results ($\tau_{\text{LO}} = 0.21$ ps [38]). Thus, in contrast with Dinh *et al.* [50], we rather conclude that the LO scattering takes place at the Γ point due to both momentum conservation and the above-discussed previous XRD results [38]. The multiple odd-number TO scattering lines correspond to TO frequencies of ≈350 cm^{-1}, which is between the frequencies of the first-order TO phonon lines (see Table I), indicating their origins as iTO(Γ) + jTO(X) ($i + j = n$) combination modes. The multiple even-number TO lines correspond to TO frequencies of ≈337 cm^{-1}, which indicates their origin as nTO(Γ) lines.

To investigate the PL signal, we scan a larger spectral range and apply lower temperatures down to 5 K. These spectra demonstrate multiphonon scattering and luminescence in a single measurement but do not allow precise evaluation of the n-phonon peak positions due to the decreased accuracy (see the Supplemental Material [36]). In Fig. 4(b), the Raman/PL spectra are presented from 1.9–2.6 eV for different temperatures. We find a broad luminescence peak with a maximum at ≈2.15 eV and multiphonon Raman signals up to 6LO and 9TO. Surprisingly, the center energy of the luminescence signal seems to decrease slightly with decreasing temperature. Accordingly, the 6LO Raman line exhibits a much larger intensity with respect to the lower-order modes at low temperature (5 K). This enhancement is caused by better matching of the resonance condition resulting from the slight decrease of the direct band gap. Comparing the luminescence peak with our ellipsometry results, we conclude that luminescence arises from direct band-to-band recombination at the X point. Concerning the band structure shown in Fig. 1, the VB seems to be only a saddle point, and photogenerated holes could easily thermalize toward Γ. Our observation thus strongly indicates a local VB maximum at the X point. For a degenerately doped ScN single crystal ($n_{\text{Hall}} = 2.2 \times 10^{21}$ cm^{-3}), Al Atabi *et al.* [47] reported angle-resolved photoemission spectroscpy (ARPES) measurements indicating such a local VB maximum at the X point.

Conclusions. In summary, we investigated a HVPE-grown quasi-bulk rs-ScN single crystal and derived fundamental material parameters which are listed in Table II (see the Supplemental Material [36] for error analysis). UV-SE precisely yields an absorption edge of $E_g = 2.16$ eV from an Elliott model fit as well as $\varepsilon_\infty = 8.3$ from a Shokhovets model fit. Additionally, an estimate of the exciton binding energy of $E_{\text{bX}} = 14$ meV was extracted. IR-SE and IR reflectivity showed a strong phonon and a weak free carrier (plasmon)

TABLE II. Overview of results. Note that ω_{LO} displays the eigenfrequency of the first-order LO signal at $E_{\text{Laser}} = 2.62$ eV. For details about the experimental accuracy see the Supplemental Material [36].

Parameter	Unit	Value	Accuracy
ω_{TO}	cm^{-1}	340.7	±0.03
γ_{TO}	cm^{-1}	3.7	±0.06
$\varepsilon_{\text{stat}}$		29.5	±0.5
ε_∞		8.3	±0.2
ω_{LO}	cm^{-1}	684.5	±2
γ_{LO} (τ_{LO})	cm^{-1} (ps)	27 (0.20)	±4 (±0.03)
$\frac{\omega_{\text{LO}}^2}{\omega_{\text{TO}}^2}\frac{\varepsilon_\infty}{\varepsilon_{\text{stat}}}$		1.14	±0.06
$\omega_{\text{LO}}^{(\text{LST})}$	cm^{-1}	640	±20
$Z^*_{\text{Sc}} = -Z^*_{\text{N}}$		3.81	±0.05
$Z^{*(\text{LST})}_{\text{Sc}} = -Z^{*(\text{LST})}_{\text{N}}$		3.50	±0.2
E_{bX}	meV	14	±1
$E_{\overline{\Gamma X}}$	eV	1.1	±0.1
E_{g}	eV	2.16	±0.002
γ_{g}	meV	76	±3
E_Γ	eV	3.75	±0.02
$E_{\Gamma'}$	eV	5.20	±0.03

absorption. Drude-Lorentz fitting yields $\omega_{\mathrm{TO}} = 340.7\,\mathrm{cm}^{-1}$, $\gamma_{\mathrm{TO}} = 3.7\,\mathrm{cm}^{-1}$, and $\varepsilon_{\mathrm{stat}} = 29.5$.

Checking the Lyddane-Sachs-Teller (LST) relation yields $\frac{\omega_{\mathrm{LO}}^2}{\omega_{\mathrm{TO}}^2}\frac{\varepsilon_\infty}{\varepsilon_{\mathrm{stat}}} = 1.14 \pm 0.06$, which is significantly off the expected value of 1. Deriving the LO frequency from LST yields $\omega_{\mathrm{LO}}^{(\mathrm{LST})} = 640 \pm 20\,\mathrm{cm}^{-1}$, which is much closer to theoretically calculated values than our Raman result. Possible reasons for this deviation are the large LO broadening, which is neglected in the LST relation, or the coupling of the LO phonon mode with free charge carriers. Born effective charges are calculated as $Z^*_{\mathrm{Sc}} = 3.81$ and $Z^{*(\mathrm{LST})}_{\mathrm{Sc}} = 3.5$ using ω_{LO} and $\omega_{\mathrm{LO}}^{(\mathrm{LST})}$, respectively.

The free carrier absorption could not be described adequately by the Drude model. From Raman scattering experiments at different excitation wavelengths, we observed efficient multiphonon scattering up to 4LO and 7TO, and even 6LO and 9TO from temperature-dependent combined Raman/PL spectroscopy. The nLO and nTO positions and broadening parameters are determined from Lorentzian line shape fits, which describe the spectra adequately for $E_{\mathrm{Laser}} = 2.62\,\mathrm{eV}$. The LO broadening parameter increases with higher scattering order n, and the determined first-order LO frequency is $\omega_{\mathrm{LO}} = 684.5\,\mathrm{cm}^{-1}$, in good agreement with previous experiments [38,53]. In a combined Raman and PL measurement, we observed a broad luminescence signal at $\approx$2.15 eV, which perfectly matches the UV-SE determined direct band gap of 2.16 eV. From this, we assume a possible local VBM at the X point in agreement with earlier ARPES measurements [47].

Acknowledgments. This letter was funded by the DFG within the framework of the priority programme 2312 (GaNius) under Projects No. 441885089 and 462722619. We acknowledge support by the project Quantum Materials for Applications in Sustainable Technologies, Project No. CZ.02.01.01/00/22_008/0004572, the Czech Science Foundation (GACR) under Project No. GA20-10377S, and the CzechNanoLab Research Infrastructure supported by MEYS CR (Project No. LM2023051). We thank Patrick Rinke for providing the DFT data.

[1] N. Takeuchi, Phys. Rev. B **65**, 045204 (2002).
[2] B. Biswas and B. Saha, Phys. Rev. Mater. **3**, 020301 (2019).
[3] N. L. Adamski, C. E. Dreyer, and C. G. van de Walle, Appl. Phys. Lett. **115**, 232103 (2019).
[4] M. A. Moram, Y. Zhang, M. J. Kappers, Z. H. Barber, and C. J. Humphreys, Appl. Phys. Lett. **91**, 152101 (2007).
[5] C. Höglund, J. Birch, B. Alling, J. Bareño, Z. Czigány, P. O. Å. Persson, G. Wingqvist, A. Zukauskaite, and L. Hultman, J. Appl. Phys. **107**, 123515 (2010).
[6] S. Satoh, K. Ohtaka, T. Shimatsu, and S. Tanaka, J. Appl. Phys. **132**, 025103 (2022).
[7] O. Ambacher, B. Christian, N. Feil, D. F. Urban, C. Elsässer, M. Prescher, and L. Kirste, J. Appl. Phys. **130**, 045102 (2021).
[8] O. Ambacher, S. Mihalic, M. Yassine, A. Yassine, N. Afshar, and B. Christian, J. Appl. Phys. **134**, 160702 (2023).
[9] S. Fichtner, N. Wolff, F. Lofink, L. Kienle, and B. Wagner, J. Appl. Phys. **125**, 114103 (2019).
[10] N. Wolff, S. Fichtner, B. Haas, M. R. Islam, F. Niekiel, M. Kessel, O. Ambacher, C. Koch, B. Wagner, F. Lofink, and L. Kienle, J. Appl. Phys. **129**, 034103 (2021).
[11] K. Frei, R. Trejo-Hernández, S. Schütt, L. Kirste, M. Prescher, R. Aidam, S. Müller, P. Waltereit, O. Ambacher, and M. Fiederle, Jpn. J. Appl. Phys. **58**, SC1045 (2019).
[12] R. Deng, B. D. Ozsdolay, P. Y. Zheng, S. V. Khare, and D. Gall, Phys. Rev. B **91**, 045104 (2015).
[13] P. Weinberger, K. Schwarz, and A. Neckel, J. Phys. Chem. Solids **32**, 2063 (1971).
[14] A. Neckel, P. Rastl, R. Eibler, P. Weinberger, and K. Schwarz, J. Phys. C: Solid State Phys. **9**, 579 (1975).
[15] D. Gall, M. Städele, K. Järrendahl, I. Petrov, P. Desjardins, R. T. Haasch, T.-Y. Lee, and J. E. Greene, Phys. Rev. B **63**, 125119 (2001).
[16] A. Qteish, P. Rinke, M. Scheffler, and J. Neugebauer, Phys. Rev. B **74**, 245208 (2006).
[17] R. Deng, P. Y. Zheng, and D. Gall, J. Appl. Phys. **118**, 015706 (2015).
[18] S. Mu, A. J. E. Rowberg, J. Leveillee, F. Giustino, and C. G. Van de Walle, Phys. Rev. B **104**, 075118 (2021).
[19] J. Dismukes, W. Yim, and V. Ban, J. Cryst. Growth **13-14**, 365 (1972).
[20] G. Travaglini, F. Marabelli, R. Monnier, E. Kaldis, and P. Wachter, Phys. Rev. B **34**, 3876 (1986).
[21] D. Gall, I. Petrov, L. D. Madsen, J.-E. Sundgren, and J. E. Greene, J. Vac. Sci. Technol. **16**, 2411 (1998).
[22] Y. Oshima, E. G. Víllora, and K. Shimamura, J. Appl. Phys. **115**, 153508 (2014).
[23] J. M. Gregoire, S. D. Kirby, G. E. Scopelianos, F. H. Lee, and R. B. van Dover, J. Appl. Phys. **104**, 074913 (2008).
[24] B. Saha, G. Naik, V. P. Drachev, A. Boltasseva, E. E. Marinero, and T. D. Sands, J. Appl. Phys. **114**, 063519 (2013).
[25] P. V. Burmistrova, J. Maassen, T. Favaloro, B. Saha, S. Salamat, Y. Rui Koh, M. S. Lundstrom, A. Shakouri, and T. D. Sands, J. Appl. Phys. **113**, 153704 (2013).
[26] B. Saha, M. Garbrecht, J. A. Perez-Taborda, M. H. Fawey, Y. R. Koh, A. Shakouri, M. Martin-Gonzalez, L. Hultman, and T. D. Sands, Appl. Phys. Lett. **110**, 252104 (2017).
[27] S. Chowdhury, R. Gupta, P. Rajput, A. Tayal, D. Rao, R. Sekhar, S. Prakash, R. Rajagopalan, S. N. Jha, B. Saha, and M. Gupta, Materialia **22**, 101375 (2022).
[28] A. R. Smith, H. A. H. AL-Brithen, D. C. Ingram, and D. Gall, J. Appl. Phys. **90**, 1809 (2001).
[29] M. A. Moram, Z. H. Barber, C. J. Humphreys, T. B. Joyce, and P. R. Chalker, J. Appl. Phys. **100**, 023514 (2006).
[30] D. Rao, B. Biswas, E. Flores, A. Chatterjee, M. Garbrecht, Y. R. Koh, V. Bhatia, A. I. K. Pillai, P. E. Hopkins, M. Martin-Gonzalez, and B. Saha, Appl. Phys. Lett. **116**, 152103 (2020).
[31] H. A. Al-Brithen, A. R. Smith, and D. Gall, Phys. Rev. B **70**, 045303 (2004).
[32] S. Kerdsongpanya, B. Alling, and P. Eklund, Phys. Rev. B **86**, 195140 (2012).
[33] Y. Kumagai, N. Tsunoda, and F. Oba, Phys. Rev. Appl. **9**, 034019 (2018).

[34] M. A. Moram, Z. H. Barber, and C. J. Humphreys, Thin Solid Films **516**, 8569 (2008).

[35] A. J. E. Rowberg, S. Mu, and C. G. van de Walle, J. Appl. Phys. **135**, 125701 (2024).

[36] See Supplemental Material at http://link.aps.org/supplemental/10.1103/PhysRevMaterials.8.L071601 for detailed experimental setups, UV-SE model fit, Raman spectrum fit results, and measurement uncertainties. Figures off all applied Lorentzian type lin shape fits to the Raman spectrum at 2.62 eV are presented as well as the dielectric function model fit to the ellipsometric angles Ψ and Δ. Also the origins of given uncertainty values for all derived parameters are discussed.

[37] T. R. Paudel and W. R. L. Lambrecht, Phys. Rev. B **79**, 085205 (2009).

[38] H. Uchiyama, Y. Oshima, R. Patterson, S. Iwamoto, J. Shiomi, and K. Shimamura, Phys. Rev. Lett. **120**, 235901 (2018).

[39] E. Burstein, F. A. Johnson, and R. Loudon, Phys. Rev. **139**, A1239 (1965).

[40] M. V. Abrashev, A. P. Litvinchuk, C. Thomsen, and V. N. Popov, Phys. Rev. B **55**, R8638(R) (1997).

[41] E. Baron, R. Goldhahn, M. Deppe, D. J. As, and M. Feneberg, Phys. Rev. Mater. **3**, 104603 (2019).

[42] S. Shokhovets, R. Goldhahn, G. Gobsch, S. Piekh, R. Lantier, A. Rizzi, V. Lebedev, and W. Richter, J. Appl. Phys. **94**, 307 (2003).

[43] M. Feneberg, J. Nixdorf, C. Lidig, R. Goldhahn, Z. Galazka, O. Bierwagen, and J. S. Speck, Phys. Rev. B **93**, 045203 (2016).

[44] X. Y. Zhang and D. Gall, Phys. Rev. B **82**, 045116 (2010).

[45] X. Gonze and C. Lee, Phys. Rev. B **55**, 10355 (1997).

[46] R. J. Elliott, Phys. Rev. **108**, 1384 (1957).

[47] H. A. Al-Atabi, X. Zhang, S. He, C. chen, Y. Chen, E. Rotenberg, and J. H. Edgar, Appl. Phys. Lett. **121**, 182102 (2022).

[48] M. S. Haseman, B. A. Noesges, S. Shields, J. S. Cetnar, A. N. Reed, H. A. Al-Atabi, J. H. Edgar, and L. J. Brillson, APL Mater. **8**, 081103 (2020).

[49] J. F. Muth, J. H. Lee, I. K. Shmagin, R. M. Kolbas, H. C. Casey, B. P. Keller, U. K. Mishra, and S. P. DenBaars, Appl. Phys. Lett. **71**, 2572 (1997).

[50] D. V. Dinh, F. Peiris, J. Lähnemann, and O. Brandt, Appl. Phys. Lett. **123**, 112102 (2023).

[51] B. Saha, J. Acharya, T. D. Sands, and U. V. Waghmare, J. Appl. Phys. **107**, 033715 (2010).

[52] A. Herwadkar and W. R. L. Lambrecht, Phys. Rev. B **79**, 035125 (2009).

[53] K. C. Maurya, D. Rao, S. Acharya, P. Rao, A. I. K. Pillai, S. K. Selvaraja, M. Garbrecht, and B. Saha, Nano Lett. **22**, 5182 (2022).